



Effect of lanthanum and chlorine doping on strontium titanates for the electrocatalytically-assisted oxidative dehydrogenation of ethane

Doruk Dogu^a, Katja E. Meyer^a, Anshuman Fuller^a, Seval Gunduz^a, Dhruba J. Deka^a, Nathaniel Kramer^a, Anne C. Co^b, Umit S. Ozkan^{a,*}

^a William G. Lowrie Department of Chemical and Biomolecular Engineering, The Ohio State University, USA

^b Department of Chemistry and Biochemistry, The Ohio State University, USA



ARTICLE INFO

Keywords:

Electrocatalytic oxidative dehydrogenation
Ethylene production
Solid oxide membrane reactor
Strontium titanate
Perovskite

ABSTRACT

Oxidative dehydrogenation (ODH) of alkanes is an important catalytic reaction that can be used to convert less valuable alkanes, such as ethane, to more valuable olefins, such as ethylene. However, further oxidation of olefins to carbon dioxide and carbon monoxide limits the selectivity of the process. Oxide ion-conducting electrolyte reactors allow for controlling oxygen availability to the reaction and thus, improve the selectivity for olefin formation. In this study, strontium titanate-type perovskites were tested as anode catalysts for electro ODH reaction. Cl-incorporated, La-doped strontium titanates were synthesized via a modified Pechini route. The effect of lanthanum doping and chlorine incorporation on these catalysts was investigated. The characteristics of the catalysts were examined using ambient and *in-situ* X-ray diffraction (XRD), X-ray photoelectron spectroscopy (XPS), diffuse reflectance infrared Fourier transform spectroscopy (DRIFTS), temperature-programmed oxidation (TPO) using CO₂, laser Raman spectroscopy, and electrical conductivity measurements. In addition, impedance measurements were also taken to better understand the cell characteristics and resistances. Electrocatalytically-assisted ODH tests on the cell with La_{0.2}Sr_{0.8}TiO₃ ± dCl_o anode showed that ethane conversion and ethylene production rates increase with increasing current. It was also observed that La doping increases the electrical conductivity and ethane conversion, while Cl doping increases both ethane conversion and ethylene selectivity.

1. Introduction

Light olefins, such as ethylene and propylene, are some of the most commercially valuable chemicals produced in the world, and are used in making a varied range of products across several industrial sectors. They are used in the manufacture of major consumer goods, from air-crafts to clothing, and their combined demand outruns that of any other chemical [1]. The most common methods for the production of these olefins are steam cracking and fluid catalytic cracking of naphtha, light diesel and other oil products [2]. These methods are very capital intensive, since the products produced have to be separated and purified after production, and demand for the products is usually not equivalent to the amount produced, so that some products are stored, adding to the overall cost [3]. An alternative method is catalytic dehydrogenation of alkanes to their corresponding olefins in the presence of a catalyst. Catalytic dehydrogenation, however, is limited by several factors, such as high endothermicity, coke formation, and thermodynamic equilibrium limitations [3–7]. Oxidative dehydrogenation (ODH) is an appealing process which may overcome the problems of catalytic

dehydrogenation [3,5,6]. ODH is similar to dehydrogenation; however, oxygen is also fed to the reactor with alkanes. Oxygen enhances the forward reaction by oxidizing the H₂ evolved during dehydrogenation to H₂O, shifts the reaction equilibrium, reduces the possibility of side reactions such as coking and cracking, and converts an endothermic process to an exothermic one, thereby enabling it to operate at lower temperatures [8–10]. Selectivity control, however, is still a major challenge, as further oxidation of the formed olefins to CO and CO₂ limits the olefin yields [4,6,11,12].



Traditionally, oxidative dehydrogenation reactions have been conducted in packed-bed reactors, in the presence of molecular oxygen or air as the oxidant [13]. In such a setup, limiting the complete oxidation reaction is a major challenge and the high oxygen partial pressures favor the formation of carbon oxides from the olefin product and even the alkane itself, decreasing the overall olefin selectivity [14]. Some

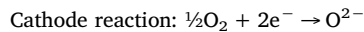
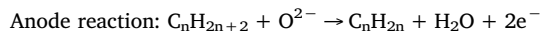
* Corresponding author.

E-mail address: ozkan.1@osu.edu (U.S. Ozkan).

studies focused on using different oxidants for ODH such as N_2O , as N_2O dissociates on the catalyst surface to form O^- species [12,15]. Ethane ODH studies using N_2O as oxidant shows that O^- ions can be used to selectively convert ethane to ethylene [12,16–18]. Thus, a reactor design which can supply reactive oxygen anions to the reaction surface may provide an advantage in terms of selectivity.

Oxide ion-conducting electrolyte reactors can be used as oxygen pumps, and the oxygen flux through the electrolyte can be controlled by the external current drawn [19,20]. These electrochemical reactors may improve the selectivity for olefin formation by controlling the current, and thus, the oxygen available for the reaction [21,22]. The reactor setup is similar to solid oxide fuel cells, with an important difference: instead of generating power as in solid oxide fuel cells, an external current is regulated to control the oxygen flux through the electrolyte. When the current is drawn, the O_2 molecules at the cathode are reduced to O^{2-} ions. These O^{2-} ions conduct through the electrolyte to the anode, and on the anode surface, oxide ions may oxidize to molecular oxygen, i.e. $\text{O}^{2-} \rightarrow \text{O}^- \rightarrow \text{O}_2^- \rightarrow \text{O}_2$ or be converted to other oxide ion species as shown in the sequence [19]. Although there are differing views in the literature as to which oxygen species leads to which reaction pathway, it is generally agreed upon that the type of oxygen species on the surface and their distributions affect the conversion and selectivity of oxidation reactions [23–26]. The majority of literature reports O^- as the most selective oxygen species for the dehydrogenation reaction [27–34]. There are also studies that observe superoxide (O_2^-) on the surface of catalysts that are active for dehydrogenation, however the possibility of O_2^- species transforming to O^- during the reaction is not ruled out [35,36]. On the other hand, Dai et al. [37] claims dioxygen species such as $\text{O}_2^{\delta-}$ ($0 < \delta < 1$), O_2^- , O_2^{n-} ($1 < n < 2$), O_2^{2-} are more selective for ethylene formation and O^- ions are responsible for complete oxidation of ethane and ethylene to CO_2 . It can also be claimed that the ionic oxygen species on the anode surface obtained by oxygen pumping through the cell are more selective for olefin and oxygenated hydrocarbon formations, whereas reactions with high concentrations of molecular oxygen primarily leads to complete oxidation to CO_2 [19,38–40]. The advantage of electrocatalytic setup using solid oxide electrolyte reactors is that ethane or ethylene never come in contact with the gas phase oxygen, which leads to complete oxidation.

In this scheme, the reactions that take place on the two electrodes are



One of the challenges in using solid electrolyte reactors is having a high O^{2-} ionic conductivity, and an active and selective anode catalyst with high electrical conductivity that can perform under high temperatures and low oxygen partial pressures, and with compatible thermal expansion coefficients to prevent delamination at the electrode/electrolyte interface. This work aims to explore strontium titanate perovskite oxides as potential electrochemical ODH catalysts for the conversion of ethane to ethylene, and specifically focuses on the effect of chlorine-incorporation in donor-doped strontium titanates of the type $\text{La}_x\text{Sr}_{1-x}\text{TiO}_3 \pm \delta$ as potential anodes. Strontium titanate (SrTiO_3) is reported to be very stable under reducing atmospheres, and La doping at the A-site (i.e. over Sr) to form $\text{La}_x\text{Sr}_{1-x}\text{TiO}_3 \pm \delta$ forms oxygen-rich planes in the crystal structure, and increases both the ionic and the electrical conductivity [41–43]. $\text{La}_x\text{Sr}_{1-x}\text{TiO}_3 \pm \delta$ materials are also known to be tolerant to sulfur poisoning and coking [41,43–45]. Goodenough and Huang [46] report that the $\text{Ti}^{4+}/\text{Ti}^{3+}$ redox couple in titanates have a low enough energy to accept electrons from the hydrocarbon for its oxidation, implying that alkane activation should be easily possible on the surface of the $\text{La}_x\text{Sr}_{1-x}\text{TiO}_3 \pm \delta$ materials. There is abundant evidence of halide enhancement, specifically impregnation of chlorine or the introduction of chlorinated compounds in ethane ODH

systems, which has led to improvements in the ethylene yields and selectivities [3,7,47–49]. Chlorine radicals formed on the surface of the catalyst are thought to lead to decomposition of ethyl radicals to ethylene [3,7]. For this reason, the effect of chlorine incorporation on lanthanum-doped strontium titanate was examined in this study.

2. Experimental

2.1. Catalyst synthesis

Lanthanum-doped strontium titanate, $\text{La}_x\text{Sr}_{1-x}\text{TiO}_3 \pm \delta$ ($x = 0, 0.1, 0.2, 0.3, 0.4, 0.5$), and chlorine-incorporated, lanthanum-doped strontium titanate, $\text{La}_x\text{Sr}_{1-x}\text{TiO}_3 \pm \delta\text{Cl}_\sigma$ ($x = 0.1, 0.2, 0.3, 0.4; \sigma \leq 3x$), catalysts were prepared via a modified-Pechini method, adapted from Lu et al. [50]. Stoichiometric amounts of $\text{La}(\text{NO}_3)_3 \cdot 6\text{H}_2\text{O}$ (99.999%, Sigma Aldrich) and $\text{Sr}(\text{NO}_3)_2$ (99.999%, Alfa Aesar) were measured and dissolved in the minimum amount of DI water required to make an aqueous solution. $\text{LaCl}_3 \cdot 7\text{H}_2\text{O}$ (99.999%, Alfa Aesar) was used as the lanthanum precursor in the synthesis of the chlorinated lanthanum-doped strontium titanates, instead of $\text{La}(\text{NO}_3)_3 \cdot 6\text{H}_2\text{O}$. Ethylene glycol ($\geq 99\%$, Sigma Aldrich) was added to a glass beaker kept in a water bath and stirred. A stoichiometric amount of $\text{Ti}(\text{OC}_3\text{H}_7)_4$ (97%, Sigma Aldrich) was added to the ethylene glycol solution while stirring and ethanol was immediately added to this beaker to prevent the oxidation of the titanium isopropoxide to titania, and the resulting clear solution was heated to 75 °C. The molar ratio of ethanol to water was 2:1. When the temperature reached 40 °C, citric acid (ACS reagent $\geq 99.5\%$, Sigma Aldrich) was added to this solution under constant stirring. The citric acid dissolved in the solution gradually with temperature. The mole ratio of metal ions to citric acid was kept at 1:3 and citric acid to ethylene glycol molar ratio was 1:4. At around 70 °C, when all the citric acid was dissolved, the metal nitrate solution was slowly introduced into the glass beaker and the resulting solution turned a transparent pale yellow. Pure NH_4OH was added drop-wise to the solution to adjust the pH to 6 and the solution was stirred at 75 °C for 4 h. The resulting gel was heated overnight at 200 °C in air to form a black powder which was then ground using a mortar and pestle and fired at 900 °C in air for 8 h to form the cubic perovskite structure.

2.2. XRD

X-ray diffraction studies for post-calcined catalysts were conducted using a Bruker D8 Advance Diffractometer with a $\text{Cu K}\alpha$ ($\lambda = 1.5046\text{\AA}$, 40 kV and 50 mA) radiation source under ambient conditions to verify the perovskite crystal structure. A step size of 0.014° was used at a dwell time of 0.5 s, and spectra were obtained between 2θ angles of 20–90°. For *in-situ* XRD studies, an Anton Parr HTK 1200 oven was assembled on the instrument, which allowed measurements to be taken under controlled atmosphere and temperature. After loading the sample in the oven, the sample chamber was vacuum-purged and then stabilized in a 5% H_2/N_2 environment for 1 h at room temperature. Spectra were collected from 25 °C to 900 °C under 5% H_2/N_2 atmosphere. The heating ramp rate was 10 °C/min and there was a set dwell time of 20 min at each temperature before the spectra were acquired. Spectra were collected from 2θ range of 30–60° at a step size of 0.014° with a dwell time of 0.5 s. Using Bragg's Law, d-spacing and unit cell volume were calculated for each temperature to find the thermal expansion coefficients of the materials.

2.3. Electrical conductivity

DC electrical conductivity of the catalyst samples was measured using the 4-probe van der Pauw technique. For the post-calcined $\text{La}_x\text{Sr}_{1-x}\text{TiO}_3 \pm \delta$ and $\text{La}_x\text{Sr}_{1-x}\text{TiO}_3 \pm \delta\text{Cl}_\sigma$ samples, the powders were first reduced at 1100 °C in 5% H_2/N_2 for 12 h. These powders were pelletized into rectangular bars using a hydraulic press and sintered in 5% H_2/N_2

at 1500 °C for 12 h to obtain dense pellets. Four silver wires (0.1 mm dia, 99.997% metals basis, Premion®, Alfa Aesar) were attached to the pellets using Pelco™ High Performance silver adhesive paste (Ted Pella), which was then dried at 93 °C for two hours. A Keithley 6220 current source was used to apply current to the outer silver leads and the corresponding voltage was measured by a Keithley 6182 sensitive nanovoltmeter from the inner leads. Measurements were taken from 200 to 600 °C in 5% H₂/N₂ to simulate the reducing nature of the anode environment. The electrical conductivity, σ , was then calculated using the formula shown below after allowing the voltage to attain a steady state value at each temperature.

$$\sigma = \left(\frac{I}{V} \right) \left(\frac{l}{A} \right)$$

I is the applied current, V is the measured voltage, l is the distance between the voltage leads and A is the cross sectional area for current flow. The reported conductivity values were averaged over multiple readings at each temperature.

2.4. TPO with CO₂

Temperature-programmed oxidation with CO₂ was performed in order to determine the relative degree of oxygen mobility and reducibility of each catalyst. SrTiO₃, La_{0.2}Sr_{0.8}TiO₃ ± δ , and La_{0.2}Sr_{0.8}TiO₃ ± δ Cl _{σ} powders were first reduced *ex-situ* under 5% H₂/N₂ for 12 h at 1100 °C. 50 mg of each powder was loaded into a quartz reactor tube, and placed inside a furnace. After an *in-situ* reduction step at 1000 °C for 1 h in 5% H₂/N₂, the catalyst bed was cooled to room temperature, and then heated at 10 °C/min under 30 sccm flow of CO₂ to 1000 °C and held for 1 h. The gas outlet from the reactor was fed to an MKS Cirrus bench-top residual gas analyzer, with mass signals of 1–100 monitored throughout the experiment.

2.5. XPS

X-ray photoelectron spectroscopy (XPS) experiments were performed to analyze the surface of SrTiO₃, La_{0.2}Sr_{0.8}TiO₃ ± δ , and La_{0.2}Sr_{0.8}TiO₃ ± δ Cl _{σ} using a Kratos Ultra Axis Spectrometer having a mono Al K α source (12 kV, 10 mA). The charge neutralizer was set at 2.1 A, a bias of 1.3 V, and a charge of 2.6 V during data collection. A survey scan was collected from 1400 eV to 0 eV (1 sweep/100 ms dwell), and spectra were collected for La 3d (8 sweeps, 450 ms), Sr 3d (8 sweeps, 200 ms), Ti 2p (8 sweeps, 200 ms), O 1s (8 sweeps, 100 ms), and Cl 2p (8 sweeps, 450 ms) regions. The binding energies for all the regions were corrected by referencing the C 1s spectra at 284.5 eV. The curves were fit using the software XPSPeak (version 4.1). Etching was performed for 1 and 2 min using an Ar⁺ ion gun on the La_{0.2}Sr_{0.8}TiO₃ ± δ Cl _{σ} catalyst. During etching, the accelerating voltage was 4 keV, pressures were approximately 3 × 10⁻⁷ Torr, and sample currents were around 1.0–1.5 μA.

2.6. DRIFTS

Diffuse reflectance infrared Fourier transform spectroscopy (DRIFTS) studies were performed using a Thermolectron Nicolet 6700 FTIR equipped with a MCT detector and a Praying Mantis chamber capable of measurements under controlled environment and temperature. Spectra were collected in the mid-infrared region of 4000–700 cm⁻¹, where molecular vibrations can be observed, with a resolution of 4 cm⁻¹. Each sample was first pretreated in 30 sccm of 10% O₂/He at 450 °C for 30 min in order to clean the surface, and then cooled down to 50 °C and stabilized for 30 min. A background scan was collected under helium at 50 °C before methanol adsorption. The methanol adsorption step was performed by first introducing methanol via bubbling 30 sccm He through pure methanol and sending it to the sample for one hour at 50 °C. The sample chamber was then flushed

with 30 sccm helium for 30 min and a spectrum was collected. A similar procedure was followed for pyridine adsorption experiments. The spectra were averaged over 512 scans.

2.7. Raman spectroscopy

Laser Raman Spectroscopy experiments were performed at room temperature using a LabRAM HR-800 Raman Spectrometer with a 100 x micropole, and an Argon ion laser (514.5 nm) as the excitation source. Prior to experiments, the spectrometer was calibrated by using a silicon reference and white light for 520.7 and 0 cm⁻¹ wavelength, respectively.

2.8. Button cell fabrication and electrocatalytic ODH reaction testing

The button cell in this context refers to the electrode-electrolyte assembly. First, the yttria-stabilized zirconia (YSZ) electrolyte (ESL electroscience) was cut into circular discs from a tape-casted sheet and densified at 1500 °C in air. The post-densification thickness of the YSZ disc was 125 μm with a 2.54 cm diameter. The anode catalyst powders were mixed with an ink vehicle (NexTech Materials) in a 60: 40 wt ratio then screen-printed onto the densified electrolyte and fired at 1400 °C in air. This was followed by screen-printing the LSM-YSZ slurry (1:1 wt. % mixture of La_{0.8}Sr_{0.2}MnO₃ and 8 mol% yttria-stabilized zirconia powders, NexTech Materials) on the other side of the YSZ disc as the cathode, followed by firing it at 1200 °C in air. The post-firing thickness of the electrode was ~25 μm. The SEM images of the anode surfaces of SrTiO₃ ± δ /YSZ, La_{0.2}Sr_{0.8}TiO₃ ± δ /YSZ and La_{0.2}Sr_{0.8}TiO₃ ± δ Cl _{σ} /YSZ assemblies (Fig. S1) and the cross-section of SrTiO₃ ± δ /YSZ assembly (Fig. S2) are given in the Supplementary Information section.

Once the button cell was ready, gold wires (0.1 mm O.D., 99.99% trace metals basis, Sigma Aldrich) were attached onto each of the electrodes using 8880-G high temperature conductive gold paste (ESL Electroscience) and dried at 100 °C in air for one hour. The gold leads acted as current collectors. These cells were placed on top of an alumina (2.54 cm O.D.) tube and sealed by pasting Schott GM 31107™ glass seal. The glass seal was dried at 125 °C and heated to 350 °C at 3 °C/min and held for 90 min to remove binders, then finally heated to 700 °C at 2 °C/min and cured for 30 min. After curing, the reactor was cooled to the test temperature of 600 °C. The gold leads were connected to a Keithley 6220 current source and Keithley 6182 voltmeter for current application and voltage measurement, respectively, via silver leads (0.64 mm O.D., 99.9% metals basis, Alfa Aesar). This setup is shown in Fig. 1. During electrocatalytic ODH reactions, 2 sccm of 5% ethane/He was sent to the anode, and the cell was kept under these conditions for 12 h to stabilize the operation parameters such as temperature and reactant flow. Stable OCV was measured to be between 1.06–1.17 V for all cells which is in good agreement with the theoretical value calculated at 600 °C using Nernst equation (1.09 V). After stabilization, current in the range of 0–5 mA was applied. The outlet of the reactor was sent to the Shimadzu GC 2014 for gas separation and analysis. Electrochemical impedance spectroscopy was performed on cells with SrTiO₃, La_{0.2}Sr_{0.8}TiO₃ ± δ , and La_{0.2}Sr_{0.8}TiO₃ ± δ Cl _{σ} anodes under 2 sccm of 5% ethane/He at 600 °C and LSM-YSZ cathodes exposed to air. Impedance was recorded under constant current of 0.5, 1, and 3 mA, in a frequency range of 10 mHz up to 100 kHz using an SP-150 Biologic Potentiostat with a VMP3B-5 Voltage Booster.

3. RESULTS & DISCUSSION

3.1. X-ray diffraction analysis

Figs. 2 and 3 show *ex-situ* powder XRD patterns of the post-calcination catalyst samples. Strontium titanate shows cubic perovskite symmetry and this structure remains intact after lanthanum doping for the samples La_{0.1}Sr_{0.9}TiO₃ ± δ , La_{0.2}Sr_{0.8}TiO₃ ± δ , La_{0.3}Sr_{0.7}TiO₃ ± δ and

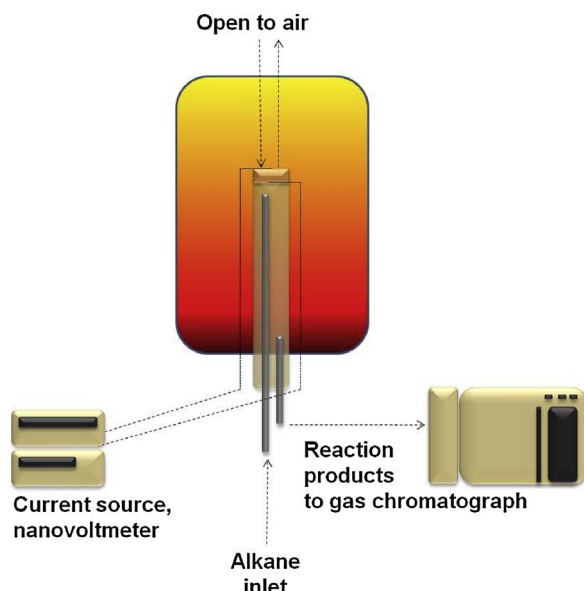


Fig. 1. Electrochemical alkane ODH reactor setup.

$\text{La}_{0.4}\text{Sr}_{0.6}\text{TiO}_3 \pm \delta$. However, separate impurity phases can be seen in the diffraction pattern of $\text{La}_{0.5}\text{Sr}_{0.5}\text{TiO}_3 \pm \delta$, possibly due to contributions from La_2TiO_5 (JCPDS 75-2394) or La_2O_3 (JCPDS 83-1348) (Fig. 2). Since lanthanum doping up to 40% at the A-site does not alter the cubic structure, the La^{2+} ions appear to be present in the perovskite oxide lattice. Similarly, the chlorine incorporated samples, $\text{La}_{0.1}\text{Sr}_{0.9}\text{TiO}_3 \pm \delta\text{Cl}_\sigma$, $\text{La}_{0.2}\text{Sr}_{0.8}\text{TiO}_3 \pm \delta\text{Cl}_\sigma$ and $\text{La}_{0.3}\text{Sr}_{0.7}\text{TiO}_3 \pm \delta\text{Cl}_\sigma$, show cubic perovskite structure indicating that the cubic perovskite structure is maintained with the chlorine incorporation (Fig. 3). Some impurity phases were present in $\text{La}_{0.4}\text{Sr}_{0.6}\text{TiO}_3 \pm \delta\text{Cl}_\sigma$, which may be due to contributions from LaOCl (JCPDS 8-0477). Presence of impurity phases might be a result of incomplete solid state reaction during calcination or co-precipitation of metal oxide phase [51]. The formation of secondary metal oxide phases with higher lanthanum doping of SrTiO_3 is well documented in the literature; however, solubility range of La in the perovskite structure varies between 40–50% in different studies [52–54]. Impurity phases appear as lanthanum- and oxygen-rich layers

separated by octahedra of the perovskite structure. At lower La doping levels, occurrence of such layers is not frequent and also not uniformly distributed, with a large number of perovskite phase octahedra being present between two impurity layers hence the resulting secondary phases are not detected by XRD. On the other hand, at higher doping levels, appearance of lanthanum- and oxygen-rich impurity layers become more frequent and they form larger clusters, thus leading to emergence of new weak peaks in the XRD pattern [52]. For Cl incorporated samples, Cl distorts the perovskite structure more than La does because of the significant ionic radius difference between oxygen and chlorine, and this might be the reason for formation of impurity phases at lower doping levels. Due to the impurity phases seen in $\text{La}_{0.5}\text{Sr}_{0.5}\text{TiO}_3 \pm \delta$ and $\text{La}_{0.4}\text{Sr}_{0.6}\text{TiO}_3 \pm \delta\text{Cl}_\sigma$, these two catalyst compositions were not considered further in this study.

Lattice parameters calculated using Braggs's Law were found to be in the range of 3.903–3.905 Å for all catalysts up to 40% lanthanum doping, and this is in good agreement with the literature [55,56]. It was also observed that the catalyst with 50% La doping has a significantly higher lattice parameter of 3.920 Å, which might be due to the distortions in the structure as well as the impurities observed for this sample.

The crystallite sizes of the catalyst samples were calculated using the Scherrer equation (Table 1). It appears that crystallite size decreases with increase in lanthanum doping which may mean that lanthanum doping inhibits crystal growth for strontium titanate, while a small increase is observed due to chlorine incorporation.

In-situ XRD patterns of SrTiO_3 , $\text{La}_{0.2}\text{Sr}_{0.8}\text{TiO}_3 \pm \delta$ and $\text{La}_{0.2}\text{Sr}_{0.8}\text{TiO}_3 \pm \delta\text{Cl}_\sigma$ were collected in temperature range of 25–800 °C under 5% H_2/N_2 . All three samples retain their cubic perovskite structure under reducing atmospheres up to 900 °C, indicating they will be stable under the operating temperature of 600 °C. *In-situ* diffraction patterns are shown for $\text{La}_{0.2}\text{Sr}_{0.8}\text{TiO}_3 \pm \delta\text{Cl}_\sigma$ (Fig. 4). The thermal expansion coefficient was calculated to be around $15 \times 10^{-6}/\text{K}$ (Fig. 4-inset). This value did not change much with the La doping level or with Cl addition. XRD patterns for other samples are not shown since there were no differences observed and the cubic structure remained intact in the entire temperature range.

3.2. Electrical conductivity

Electrical conductivity is an important property for any material

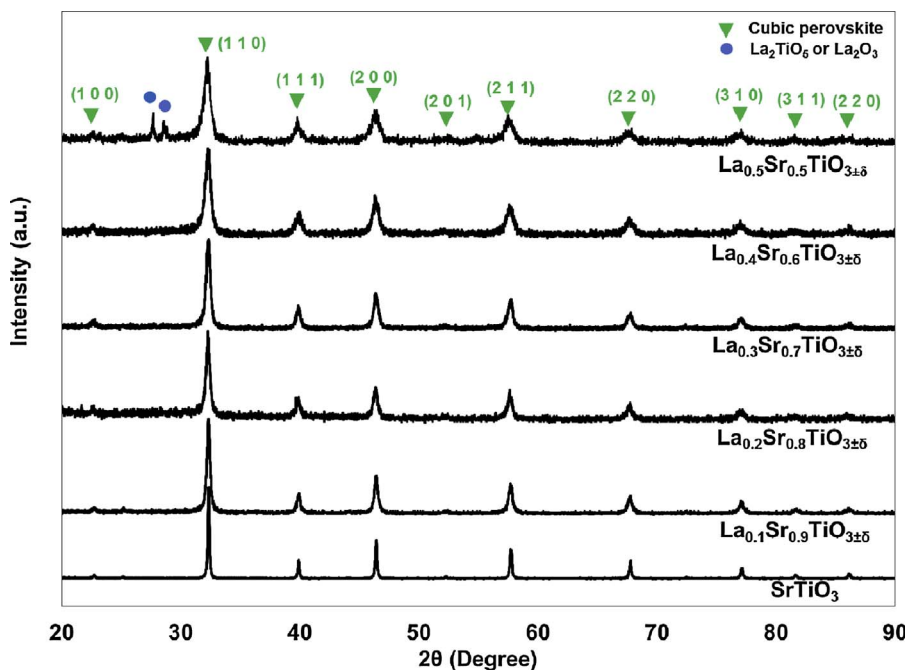


Fig. 2. *Ex-situ* XRD patterns of lanthanum-doped strontium titanates collected under ambient conditions.

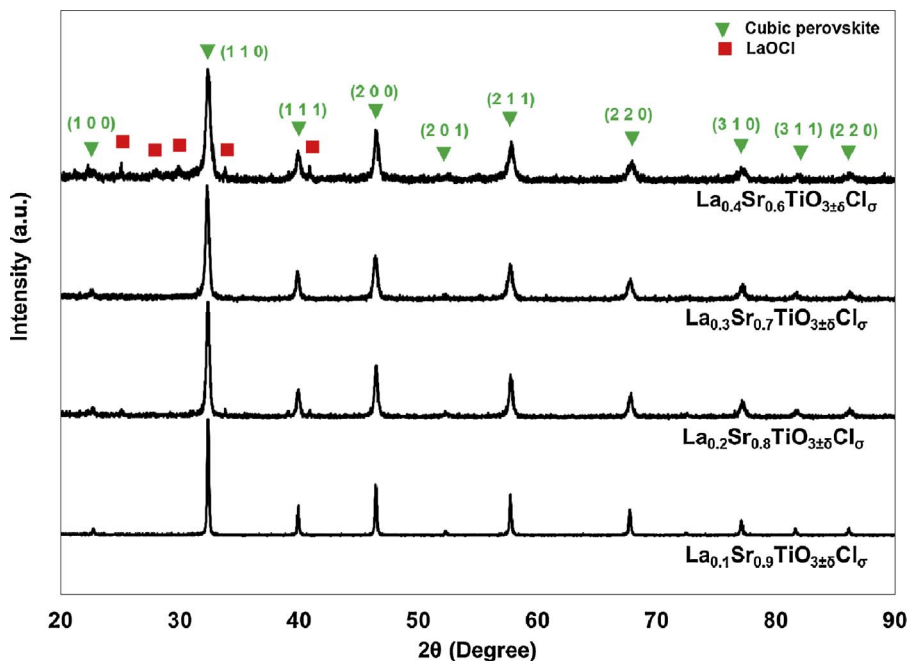


Fig. 3. Ex-situ XRD patterns of chlorine-incorporated, lanthanum-doped strontium titanates collected under ambient conditions.

Table 1
Crystal size of catalyst samples.

Catalyst	Crystal Size (nm)	Catalyst	Crystal size (nm)
SrTiO ₃	53.9	La _{0.5} Sr _{0.5} TiO ₃ ± δ	15.7
La _{0.1} Sr _{0.9} TiO ₃ ± δ	26.5	La _{0.1} Sr _{0.9} TiO ₃ ± δCl _σ	28.0
La _{0.2} Sr _{0.8} TiO ₃ ± δ	20.5	La _{0.2} Sr _{0.8} TiO ₃ ± δCl _σ	26.7
La _{0.3} Sr _{0.7} TiO ₃ ± δ	20.7	La _{0.3} Sr _{0.7} TiO ₃ ± δCl _σ	23.4
La _{0.4} Sr _{0.6} TiO ₃ ± δ	16.8	La _{0.4} Sr _{0.6} TiO ₃ ± δCl _σ	20.0

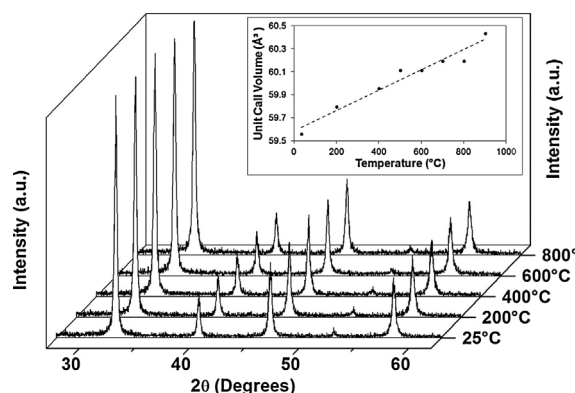


Fig. 4. In-situ XRD patterns of La_{0.2}Sr_{0.8}TiO₃ ± δCl_σ collected in a 5% H₂/N₂ environment. Inset: Change in the unit cell volume with temperature, for calculating thermal expansion coefficient.

that will be used as an electrode. If the conductivity is low, the electrochemical cell will have high resistance, limiting the power output and generating significant amount of heat [46,57]. In La_xSr_{1-x}TiO₃ ± δ materials, La doping into the A-site causes Ti⁴⁺ to become Ti³⁺, leading to enhanced electrical conductivity [58]. Conductivity of La_xSr_{1-x}TiO₃ ± δ materials of different doping levels have been studied for different environments, as well as for a variety of preparation methods [58–62]. The values obtained vary widely depending not only on the environment in which the conductivity was measured (i.e. reducing or oxidizing), but also on how the catalyst pellet was prepared [58,59]. The environment present when the pellet was sintered, for example, affects the conductivity values measured. In this study,

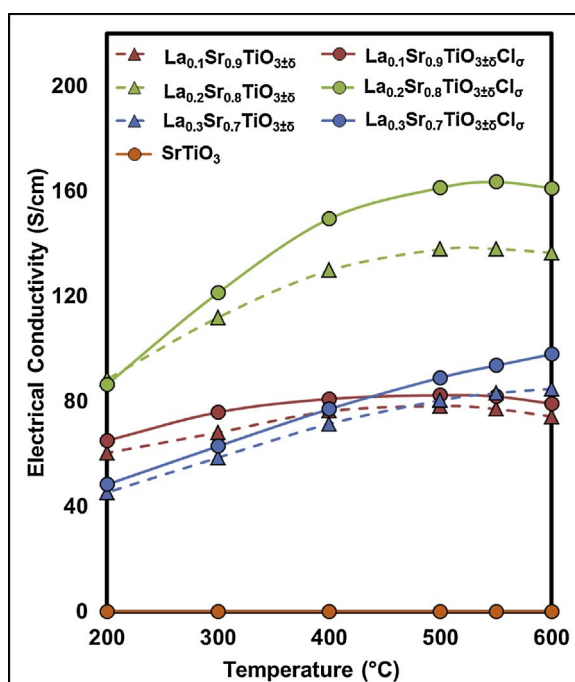


Fig. 5. Electrical conductivity for La_xSr_{1-x}TiO₃ ± δ and La_xSr_{1-x}TiO₃ ± δCl_σ catalysts between 200 and 600 °C under 5% H₂ in N₂.

catalyst pellets were subjected to a reducing environment of 5% H₂/N₂ for both the sintering step and conductivity measurement.

Conductivity measurements were obtained for La_xSr_{1-x}TiO₃ ± δ as well as La_xSr_{1-x}TiO₃ ± δCl_σ. As shown in Fig. 5, SrTiO₃ gives extremely low conductivity values (~0.05 S/cm), orders of magnitude less than catalysts doped with La. La doping greatly increases the conductivity of the titanate, as expected, giving values between 40 and 160 S/cm in all dopant levels tested. There is not, however, a positive correlation between increasing La doping level and conductivity values. The 10% and 30% La-doped catalysts, both with and without chlorine, give similar conductivity values, in the range of 40–80 S/cm. Interestingly, catalysts with 20% La doping significantly outperform the others;

$\text{La}_{0.2}\text{Sr}_{0.8}\text{TiO}_3 \pm \delta$ and $\text{La}_{0.2}\text{Sr}_{0.8}\text{TiO}_3 \pm \delta\text{Cl}_\sigma$ give the highest electrical conductivity values at all temperatures, and show maximum electrical conductivity at 550 °C of approximately 160 and 140 S/cm, respectively. This may indicate that 20% A-site doping provides an optimum in terms of electrical properties in this catalyst structure. This trend with La doping may be due to small levels of impurity phases precipitating out of the structure hindering electrical conduction in La levels higher than 20%. Although impurities are not observed in XRD after synthesis, it is possible that pellet densification led to the formation of another phase, or that a very small amount of a different phase, below the XRD detection limit, exists in the catalyst structure that significantly influences the conductivity of these materials.

The conductivity of the corresponding Cl-incorporated catalysts is slightly lower than that of their non-chlorine containing counterparts, but with similar trends. In all 10 and 20% A-site doped catalysts, an increase in conductivity is observed from 200 °C to 500 °C, before reaching a maximum at 500 and 550 °C for the 10 and 20% La-doped catalysts, respectively. In the case of $\text{La}_{0.3}\text{Sr}_{0.7}\text{TiO}_3 \pm \delta$ and $\text{La}_{0.3}\text{Sr}_{0.7}\text{TiO}_3 \pm \delta\text{Cl}_\sigma$, the values continue increasing throughout the entire temperature range, although the rate of increase is not constant. The trend with temperature in this data shows that the ideal operating range may be 500–600 °C, in which the electrical conductivity is highest, as it is such an important property for the anode catalyst in an electrochemical cell. Based on the conductivity performance, it appears that $\text{La}_{0.2}\text{Sr}_{0.8}\text{TiO}_3 \pm \delta$ and $\text{La}_{0.2}\text{Sr}_{0.8}\text{TiO}_3 \pm \delta\text{Cl}_\sigma$ are the most promising materials to be used as electrocatalysts.

3.3. TPO with CO₂

Oxygen mobility is an indicator for catalyst activity and selectivity [63,64] since oxygen ions in the lattice are involved in ODH reaction [65–68]. Oxygen ion mobility is also important for oxygen ion conductivity of the electrode in solid oxide electrolytic cells (SOECs) [57,69,70]. TPO was performed using CO₂ as the oxidant on SrTiO₃, $\text{La}_{0.2}\text{Sr}_{0.8}\text{TiO}_3 \pm \delta$, and $\text{La}_{0.2}\text{Sr}_{0.8}\text{TiO}_3 \pm \delta\text{Cl}_\sigma$ catalysts to understand their reducibility and oxygen mobility (Fig. 6). During the TPO with carbon dioxide, CO₂ is dissociated into CO and O species. While CO is detected and monitored in the gas phase by MS, oxygen species are consumed to

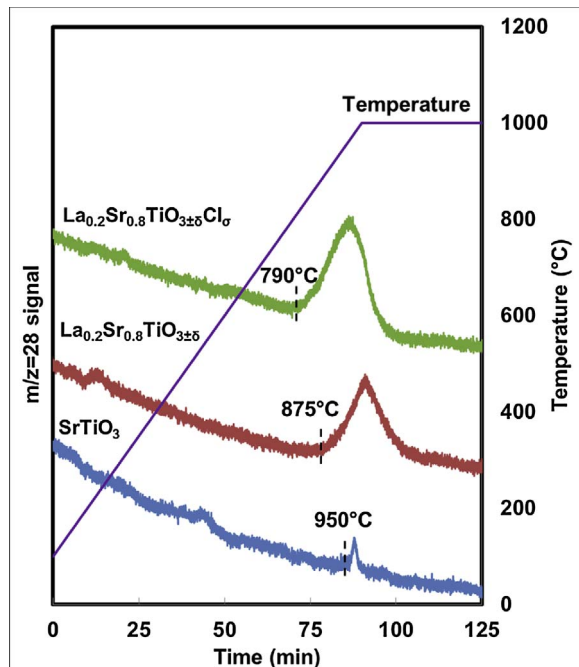


Fig. 6. Mass signal for $m/z = 28$ for SrTiO_3 , $\text{La}_{0.2}\text{Sr}_{0.8}\text{TiO}_3 \pm \delta$, and $\text{La}_{0.2}\text{Sr}_{0.8}\text{TiO}_3 \pm \delta\text{Cl}_\sigma$ during temperature-programmed oxidation with CO₂.

reoxidize the reduced catalyst. The oxygen consumed in this step is used to fill the oxygen vacancies created by partial reduction of the catalyst with hydrogen. Although the CO formation and hence the oxygen uptake is a direct function of the extent of reduction, both reduction and reoxidation steps involve conduction of oxide ions through the perovskite lattice and hence are related to oxygen mobility, as reported earlier in the literature [71–73].

It can be seen that the oxidation with CO₂ occurs at a lower temperature for the $\text{La}_{0.2}\text{Sr}_{0.8}\text{TiO}_3 \pm \delta\text{Cl}_\sigma$ catalyst (onset of 790 °C) when compared to the others. The onset temperatures for CO peaks are observed at 950 °C and 875 °C for SrTiO₃ and $\text{La}_{0.2}\text{Sr}_{0.8}\text{TiO}_3 \pm \delta$, respectively. Because oxidation of the catalyst involves oxygen movement into the lattice, a lower oxidation temperature would indicate a higher oxygen mobility. Also, the larger CO signal observed over the $\text{La}_{0.2}\text{Sr}_{0.8}\text{TiO}_3 \pm \delta\text{Cl}_\sigma$ shows a higher extent of reduction, which can also be a function of the oxygen mobility in the lattice, since reduction is not limited to the surface only. Therefore, the results of TPO with CO₂ show that $\text{La}_{0.2}\text{Sr}_{0.8}\text{TiO}_3 \pm \delta\text{Cl}_\sigma$ has a higher oxygen mobility compared to SrTiO₃ and $\text{La}_{0.2}\text{Sr}_{0.8}\text{TiO}_3 \pm \delta$, and that lanthanum doping increases oxygen mobility, as does chlorine incorporation.

3.4. XPS

The surface properties of the synthesized materials were determined using XPS. The XPS spectra for C 1s, O 1s, Ti 2p, Cl 2p, La 3d and Sr 3d regions of SrTiO₃, $\text{La}_{0.2}\text{Sr}_{0.8}\text{TiO}_3 \pm \delta$ and $\text{La}_{0.2}\text{Sr}_{0.8}\text{TiO}_3 \pm \delta\text{Cl}_\sigma$ samples were collected. La 3d and Ti 2p spectra of $\text{La}_{0.2}\text{Sr}_{0.8}\text{TiO}_3 \pm \delta\text{Cl}_\sigma$ are shown in Fig. 7a and b, respectively and were identical in all samples. All samples show titanium in a Ti^{+4} state, and the absence of the peak at around 459.5 eV which corresponds to TiO_2 [74] suggests that Ti existed in a perovskite structure only. The position of the La 3d_{5/2} and 3d_{3/2} peaks and multiplet splitting seen in La 3d region of $\text{La}_{0.2}\text{Sr}_{0.8}\text{TiO}_3 \pm \delta$ (not shown) and $\text{La}_{0.2}\text{Sr}_{0.8}\text{TiO}_3 \pm \delta\text{Cl}_\sigma$ (Fig. 7a) agree with the reported values for La⁺ [75–77]. Double splitting in La 3d spectra is due to a) spin-orbit interaction: La 3d_{5/2} and La 3d_{3/2} peaks at 834 eV and 850.7 eV, respectively; and b) transfer of an electron from the oxygen ligands to the empty La 4f level: the satellite peaks originated from this additional splitting are observed at 838.4 eV and 855.1 eV which belong to La 3d_{5/2} and La 3d_{3/2} components of La⁺, respectively. The XPS spectra for Sr 3d and O 1s regions are shown in Figs. 8 and 9, respectively, and Cl 2p region of $\text{La}_{0.2}\text{Sr}_{0.8}\text{TiO}_3 \pm \delta\text{Cl}_\sigma$ in Fig. 10. The spectra taken in the Sr 3d region (Fig. 8) show that Sr exists in two different matrices in all samples. The peak at lower binding energy (132.4 eV) corresponds to Sr^{+2} in the perovskite phase, and the peak at higher binding energy (133.2 eV) can be attributed to Sr in a sub-oxide phase ($\text{SrO}_{1-\delta}$) [78,79]. The O 1s region of the XPS spectra, shown in Fig. 9, exhibits two distinct oxygen species. The lowest binding energy peak at 529 eV corresponds to lattice oxide ions in the perovskite structure, while the peak at 530.7 eV can be attributed to adsorbed oxygen or a hydroxyl group on the surface [80,81].

Fig. 10 shows the Cl 2p spectra taken over the $\text{La}_{0.2}\text{Sr}_{0.8}\text{TiO}_3 \pm \delta\text{Cl}_\sigma$ sample. Cl existed in two different forms: the low binding energy peak at 198 eV can be assigned to anionic Cl (Cl⁻) in the perovskite structure, and the peak at 199 eV could possibly be due to surface Cl deposited as LaCl_3 [82,83]. In order to investigate the presence of Cl in the inner layers and the changes in the ratio of Cl in the perovskite structure and surface Cl, the catalyst surface was etched with an Ar⁺ gun for 1 min and 2 min. In Fig. 10, it can be seen that Cl in the perovskite structure is also present in the inner layers and the amount of Cl deposited as LaCl_3 decreases with etching. It is possible that both of these Cl species may play a role in the catalytic activity of $\text{La}_{0.2}\text{Sr}_{0.8}\text{TiO}_3 \pm \delta\text{Cl}_\sigma$. The study conducted by Dai et al. [26] showed that Cl incorporation into the structure of perovskite-type $\text{SrCo}_{3-\delta}$ increases its ethylene selectivity from 55% to 83% at 600 °C, although the surface species of chlorine are not directly identified. The peak observed at the binding energy of 195.2 is a contribution of La 4p region

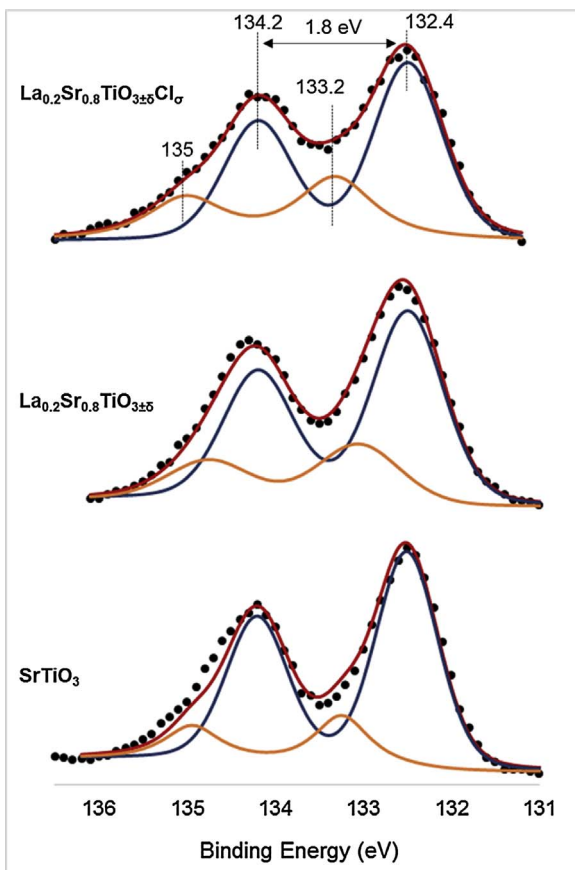
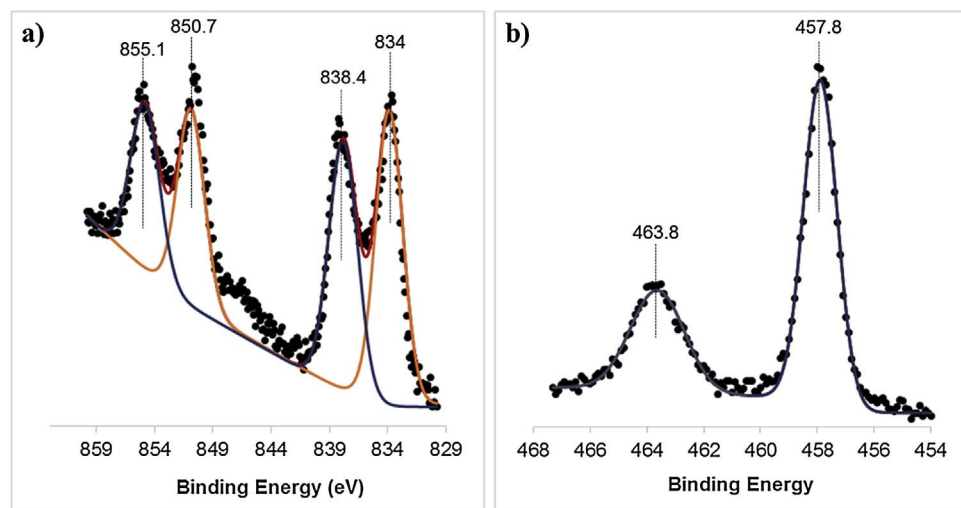


Fig. 8. X-ray photoelectron spectra of Sr 3d region for SrTiO_3 , $\text{La}_{0.2}\text{Sr}_{0.8}\text{TiO}_{3\pm\delta}$, and $\text{La}_{0.2}\text{Sr}_{0.8}\text{TiO}_{3\pm\delta}\text{Cl}_\sigma$.

and is not a part of Cl 2p spectrum [84].

3.5. Methanol and pyridine DRIFTS

Methanol and pyridine are commonly used probe molecules which can help identify the types of active sites on the surface of a catalyst [85–87]. Methanol as a probe molecule can show both basic and acidic sites depending on the variety of species formed via surface interaction [88]. Pyridine can be used to identify the presence of Lewis acid sites, as well as weak and strong Brønsted acid sites, differentiated by co-ordinated pyridine, hydrogen-bonded pyridine, and the pyridinium ion,

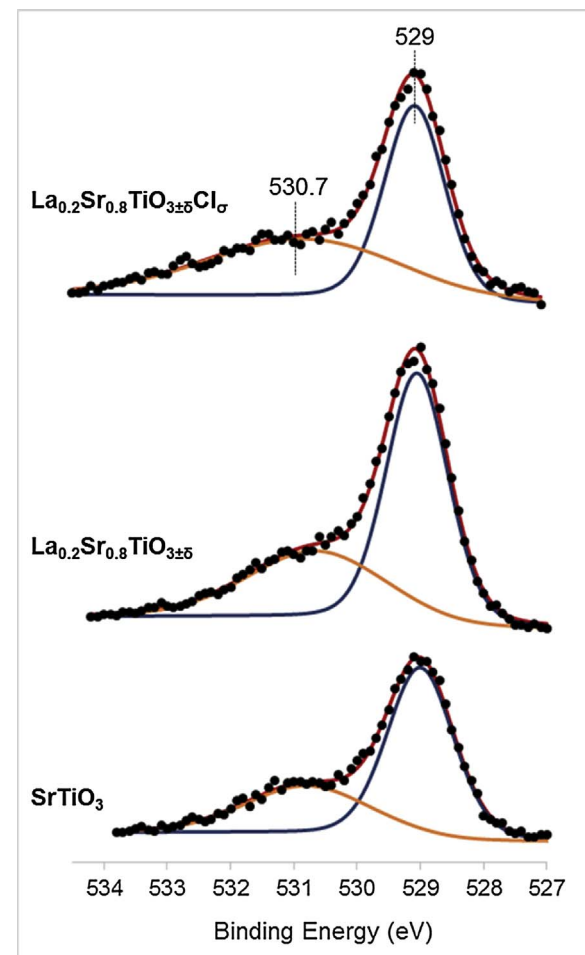


Fig. 9. X-ray photoelectron spectra of O 1s region for SrTiO_3 , $\text{La}_{0.2}\text{Sr}_{0.8}\text{TiO}_{3\pm\delta}$, and $\text{La}_{0.2}\text{Sr}_{0.8}\text{TiO}_{3\pm\delta}\text{Cl}_\sigma$.

respectively [89,90]. For each probe molecule, the cell was flushed with helium after the adsorption step, so that there is no gas phase contribution of the probe molecules and all vibrational bands observed correspond directly to species on the catalyst surfaces.

After methanol adsorption, a number of vibrational bands were observed in both the high and low wavenumber regions. In the high wavenumber region, shown in Fig. 11a, SrTiO_3 gave vibrational bands at 2810, 2832, 2916, 2943, and 3008 cm^{-1} . The bands at these

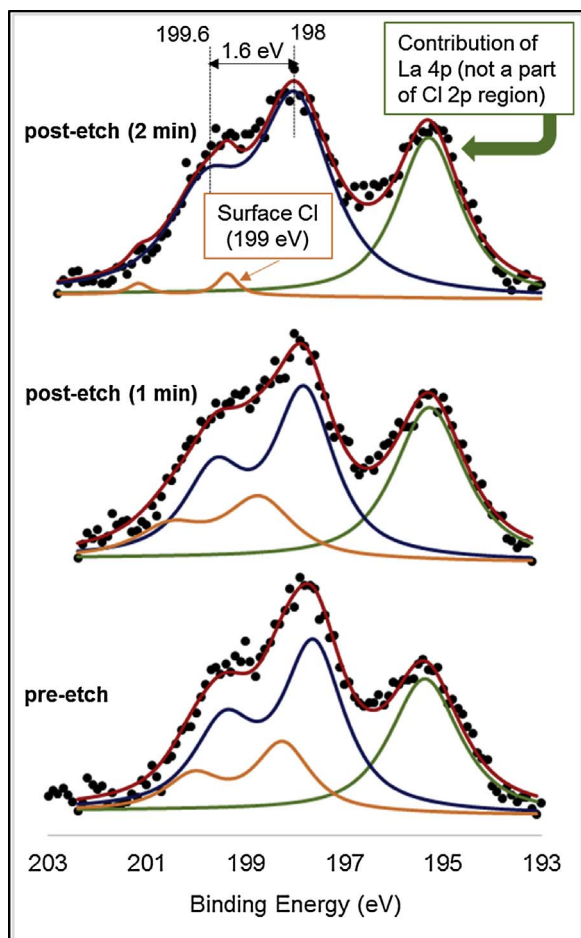


Fig. 10. X-ray photoelectron spectra of Cl 2p region for $\text{La}_{0.2}\text{Sr}_{0.8}\text{TiO}_3 \pm 8\text{Cl}_\sigma$.

wavenumbers can be assigned to $-\text{CH}_3$ stretching and bending vibrations of methoxy species; specifically, the band at 2943 cm^{-1} corresponds to a Lewis-bound symmetric $-\text{CH}_3$ stretching vibration, while that at 2832 cm^{-1} is due to a symmetric Lewis-bound $-\text{CH}_3$ bending vibration [91,92]. The bands due to symmetric stretching and bending vibrations of other surface methoxy species are seen at 2916 and 2810 cm^{-1} , respectively, while an asymmetric $-\text{CH}_3$ stretching vibration is observed at 3008 cm^{-1} [91,92]. In the low wavenumber region

(Fig. 11b), bands for other vibrational modes of $-\text{CH}_3$, as well as hydroxyl and carbonyl groups, were observed. The presence of an $-\text{OH}$ bending vibration at 1344 cm^{-1} and $-\text{CO}$ stretching vibrations at 1031 and 1053 cm^{-1} reinforce the presence of dissociatively-adsorbed methanol species [91]. In addition to these bands, $-\text{CH}_3$ rocking vibrations at 1159 and 1090 cm^{-1} are also observed.

$\text{La}_{0.2}\text{Sr}_{0.8}\text{TiO}_3 \pm 8$ shows similar vibrations as SrTiO_3 , indicating the presence of both Lewis-bound species as well as dissociatively-adsorbed, surface methoxy groups. However, lanthanum doping does change the relative intensity of the bands corresponding to the types of methoxy species. The $-\text{CH}_3$ stretching and bending vibrations of Lewis-bound species have a higher relative intensity than those for dissociatively-adsorbed surface species, indicating a higher relative abundance of Lewis acid sites in $\text{La}_{0.2}\text{Sr}_{0.8}\text{TiO}_3 \pm 8$. In $\text{La}_{0.2}\text{Sr}_{0.8}\text{TiO}_3 \pm 8\text{Cl}_\sigma$, the bands for Lewis-bound $-\text{CH}_3$ are also more intense than those for surface $-\text{CH}_3$ groups, similar to $\text{La}_{0.2}\text{Sr}_{0.8}\text{TiO}_3 \pm 8$, but to a higher degree. Thus, lanthanum doping may cause the formation of additional Lewis acid sites, and it appears that chlorine addition enhances this effect. Additionally, the bands observed in SrTiO_3 and $\text{La}_{0.2}\text{Sr}_{0.8}\text{TiO}_3 \pm 8$ at 2832 and 2943 cm^{-1} were shifted to higher wavenumbers of 2843 and 2948 cm^{-1} , respectively, in $\text{La}_{0.2}\text{Sr}_{0.8}\text{TiO}_3 \pm 8\text{Cl}_\sigma$. The shift observed for Lewis-bound methoxy species in $\text{La}_{0.2}\text{Sr}_{0.8}\text{TiO}_3 \pm 8\text{Cl}_\sigma$ to higher wavenumber indicates weaker interactions between the surface and the methanol species. According to these results, it can be stated that $\text{La}_{0.2}\text{Sr}_{0.8}\text{TiO}_3 \pm 8\text{Cl}_\sigma$ has weaker, but higher number of Lewis acidic sites.

Each catalyst exhibits a heterogeneous surface as evidenced by the formation of Lewis-bound species as well as dissociatively-adsorbed, surface methoxy groups. Dissociatively-adsorbed methanol (i.e. the methoxy surface species) is thought to be the result of interaction with a basic site on the surface, while the molecularly-adsorbed, Lewis-bound species are created because of a Lewis acid site [92]. Therefore, the surfaces of the $\text{La}_{x}\text{Sr}_{1-x}\text{TiO}_3 \pm 8$ catalysts show both Lewis acid and basic nature. Skoufa et al. [93] also observed similar sites on the surface after methanol adsorption on an oxide catalyst which was found to be active for ethane ODH.

After pyridine adsorption at 50°C , vibrational bands corresponding to pyridine species were observed in the 1400 – 1650 cm^{-1} region (Fig. 12). SrTiO_3 gives vibrational bands at approximately 1585 , 1571 , and 1439 cm^{-1} . The vibrational band observed at 1585 cm^{-1} can be attributed to coordinated pyridine, while those at 1439 and 1571 cm^{-1} may be due to either coordinated or hydrogen-bonded pyridine. Bands for coordinated pyridine may appear at approximately 1440 – 1460 , 1488 – 1503 , 1580 , and 1600 – 1633 cm^{-1} and indicate Lewis acid sites

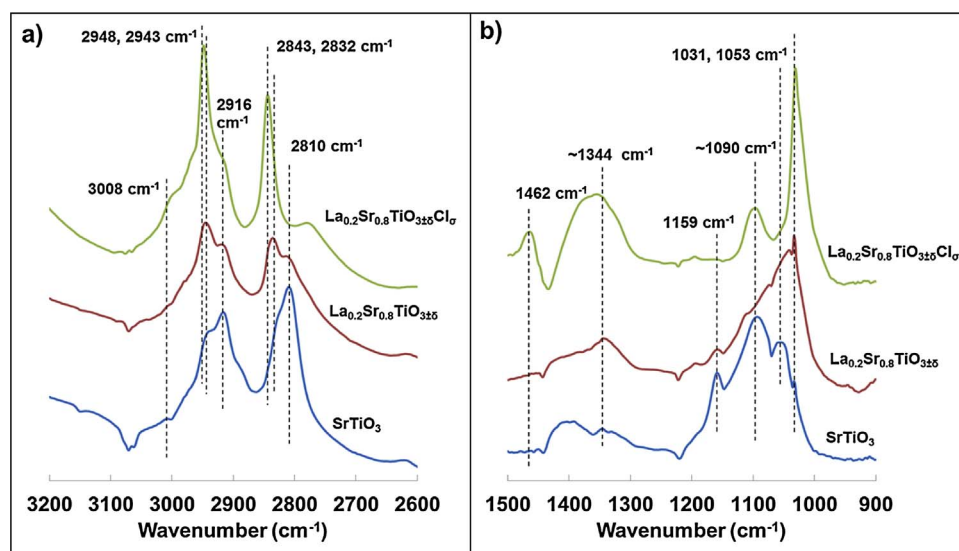


Fig. 11. DRIFTS spectra of SrTiO_3 , $\text{La}_{0.2}\text{Sr}_{0.8}\text{TiO}_3 \pm 8$, and $\text{La}_{0.2}\text{Sr}_{0.8}\text{TiO}_3 \pm 8\text{Cl}_\sigma$ for the (a) high wavenumber and (b) low wavenumber regions after methanol adsorption at 50°C .

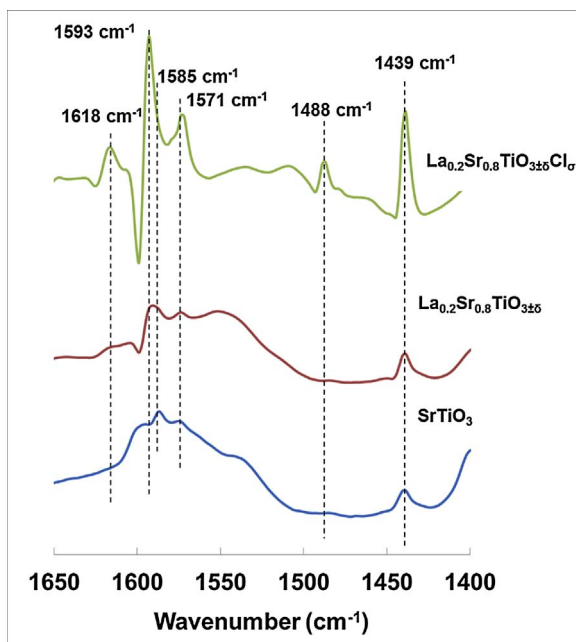


Fig. 12. DRIFTS spectra of SrTiO_3 , $\text{La}_{0.2}\text{Sr}_{0.8}\text{TiO}_{3 \pm \delta}$, and $\text{La}_{0.2}\text{Sr}_{0.8}\text{TiO}_{3 \pm \delta}\text{Cl}_\sigma$ after pyridine adsorption at 50°C .

[89,90,94]. Weak Brønsted acid sites are shown by hydrogen-bonded pyridine, which gives bands in the ranges of 1440–1447, 1485–1490, and $1580\text{--}1600\text{ cm}^{-1}$ [90,94]. Therefore, SrTiO_3 has both Lewis acid and weak Brønsted acid sites. $\text{La}_x\text{Sr}_{1-x}\text{TiO}_{3 \pm \delta}$ also gives the same bands shown in SrTiO_3 , as well as a band at approximately 1593 cm^{-1} , which is associated with coordinated pyridine. $\text{La}_{0.2}\text{Sr}_{0.8}\text{TiO}_{3 \pm \delta}\text{Cl}_\sigma$ also shows vibrational bands at 1439, 1571, 1585, and 1593 cm^{-1} as in SrTiO_3 and $\text{La}_x\text{Sr}_{1-x}\text{TiO}_{3 \pm \delta}$, as well as bands at 1488 and 1618 cm^{-1} , which correspond to hydrogen-bonded and coordinated pyridine, respectively. Based on these band assignments, all the catalysts demonstrate both Lewis acid (as evidenced by the coordinated pyridine) and weak Brønsted acid (as shown by the hydrogen-bonded pyridine) nature in their surface features, although the weak Brønsted acid nature is much more distinct in $\text{La}_{0.2}\text{Sr}_{0.8}\text{TiO}_{3 \pm \delta}\text{Cl}_\sigma$ than the others. The pyridinium ion, which indicates the presence of strong Brønsted acid sites, gives bands at approximately 1630 and 1540 cm^{-1} [89,90,95]. In the $\text{La}_x\text{Sr}_{1-x}\text{TiO}_{3 \pm \delta}$ materials, these bands were not observed, indicating they do not have a strong Brønsted acid nature. Pyridine DRIFTS experiments, similar to methanol, support the presence of Lewis acid sites on the surface of each catalyst. It is also clear that SrTiO_3 , $\text{La}_{0.2}\text{Sr}_{0.8}\text{TiO}_{3 \pm \delta}$, and $\text{La}_{0.2}\text{Sr}_{0.8}\text{TiO}_{3 \pm \delta}\text{Cl}_\sigma$ are similar materials with heterogeneous surfaces containing Lewis acid, Brønsted acid and basic sites, and the number of Lewis acid and Brønsted acid sites increases with lanthanum doping and chlorine incorporation.

3.6. Raman spectroscopy

Fig. 13 shows the Raman spectra of SrTiO_3 , $\text{La}_{0.2}\text{Sr}_{0.8}\text{TiO}_{3 \pm \delta}$, and $\text{La}_{0.2}\text{Sr}_{0.8}\text{TiO}_{3 \pm \delta}\text{Cl}_\sigma$ catalysts. A peak at 1124 cm^{-1} was observed for $\text{La}_{0.2}\text{Sr}_{0.8}\text{TiO}_{3 \pm \delta}\text{Cl}_\sigma$, which can be associated with superoxide O_2^- [96,97]. It is also observed that this peak might be present in $\text{La}_{0.2}\text{Sr}_{0.8}\text{TiO}_{3 \pm \delta}$ spectra as well; however, its intensity is much lower and hard to distinguish. No signs of superoxide ions were observed in strontium titanate from the Raman spectra collected.

3.7. Electrocatalytic ODH and electrochemical impedance spectroscopy measurements

Electrocatalytically-assisted ODH tests were conducted on cells with

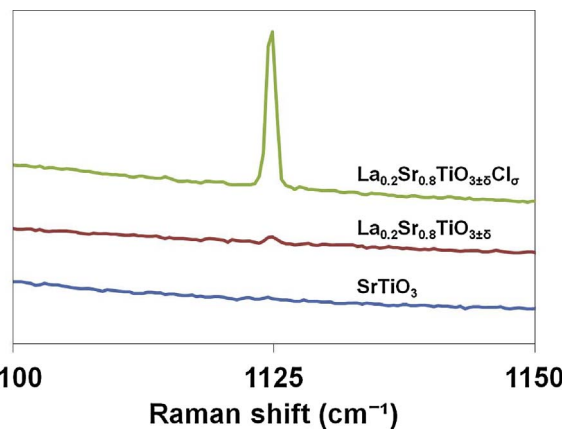


Fig. 13. Raman spectra of SrTiO_3 , $\text{La}_{0.2}\text{Sr}_{0.8}\text{TiO}_{3 \pm \delta}$, and $\text{La}_{0.2}\text{Sr}_{0.8}\text{TiO}_{3 \pm \delta}\text{Cl}_\sigma$.

SrTiO_3 , $\text{La}_{0.2}\text{Sr}_{0.8}\text{TiO}_{3 \pm \delta}$, and $\text{La}_{0.2}\text{Sr}_{0.8}\text{TiO}_{3 \pm \delta}\text{Cl}_\sigma$ as anode catalysts. Fig. 14 shows that conversion of ethane increases with applied current. It was also observed that lanthanum doping as well as chlorine incorporation increases the conversion of ethane, as $\text{La}_{0.2}\text{Sr}_{0.8}\text{TiO}_{3 \pm \delta}$ has higher conversion levels than that of the undoped strontium titanate, and $\text{La}_{0.2}\text{Sr}_{0.8}\text{TiO}_{3 \pm \delta}\text{Cl}_\sigma$ has the highest conversion levels. When the CO_x and ethylene yields are compared, it is clear that lanthanum doping and chlorine incorporation influence the conversion and selectivity. Fig. 14 shows that $\text{La}_{0.2}\text{Sr}_{0.8}\text{TiO}_{3 \pm \delta}$ is more selective for CO_x formation instead of ethylene. On the other hand, when chlorine is incorporated in the lanthanum-doped strontium titanate catalyst, besides the increase in ethane conversion, selectivity changes drastically to favor ethylene formation over CO_x . Amongst the catalysts investigated, it was observed that $\text{La}_{0.2}\text{Sr}_{0.8}\text{TiO}_{3 \pm \delta}\text{Cl}_\sigma$ has the highest ethane conversion, ethylene yield and selectivity. The superoxide ions observed on $\text{La}_{0.2}\text{Sr}_{0.8}\text{TiO}_{3 \pm \delta}\text{Cl}_\sigma$ catalyst in Raman spectroscopy might have an effect on higher selectivity towards ethylene formation, however to determine the active oxygen species on the surface under reaction condition and to understand their effect on activity, in-situ and operando characterizations should be carried out. In order to verify that the activity difference of the materials is not due to the differences in surface areas of the materials, BET surface area analysis was performed on all the samples, which were fired at 1400°C (firing temperature of the cells). It was found that the surface areas of the samples were remarkably similar ($\sim 1\text{ m}^2/\text{g}$). Therefore, we can confidently say that the differences observed in activity are not due to the differences in surface areas.

Electrochemical activity data collected between 550°C and 600°C , was used for calculating the activation energy for ethane conversion. For easier calculations, we assumed constant reactant concentrations over the electrodes under investigation. At 0.5 mA current, the activation energies for SrTiO_3 and $\text{La}_{0.2}\text{Sr}_{0.8}\text{TiO}_{3 \pm \delta}\text{Cl}_\sigma$ were 56 and 34 kJ/mol , respectively. At 5 mA , these values were 24 and 21 kJ/mol , respectively, with a $\pm 10\%$ error margin. These values appear to be significantly lower than the activation energies reported in non-electrocatalytic studies for ODH of ethane, which are in the range of $70\text{--}160\text{ kJ/mol}$ [98–101].

The total Faradic efficiencies of CO , CO_2 , and ethylene were calculated for 5 mA and found to be around $40 \pm 5\%$ for SrTiO_3 , $100 \pm 15\%$ for $\text{La}_{0.2}\text{Sr}_{0.8}\text{TiO}_{3 \pm \delta}$ and $80 \pm 10\%$ for $\text{La}_{0.2}\text{Sr}_{0.8}\text{TiO}_{3 \pm \delta}\text{Cl}_\sigma$ catalysts. It should be noted that since water formation was not quantified in these experiments, an accurate calculation of the Faradaic efficiencies was not possible.

Fig. 15 compares the voltages at each current for the cells containing SrTiO_3 , $\text{La}_{0.2}\text{Sr}_{0.8}\text{TiO}_{3 \pm \delta}$, and $\text{La}_{0.2}\text{Sr}_{0.8}\text{TiO}_{3 \pm \delta}\text{Cl}_\sigma$ anodes. It is observed that the voltages for the cells with $\text{La}_{0.2}\text{Sr}_{0.8}\text{TiO}_{3 \pm \delta}$ and $\text{La}_{0.2}\text{Sr}_{0.8}\text{TiO}_{3 \pm \delta}\text{Cl}_\sigma$ anodes are similar to each other, whereas that of the cell with SrTiO_3 anode is significantly higher for the same current

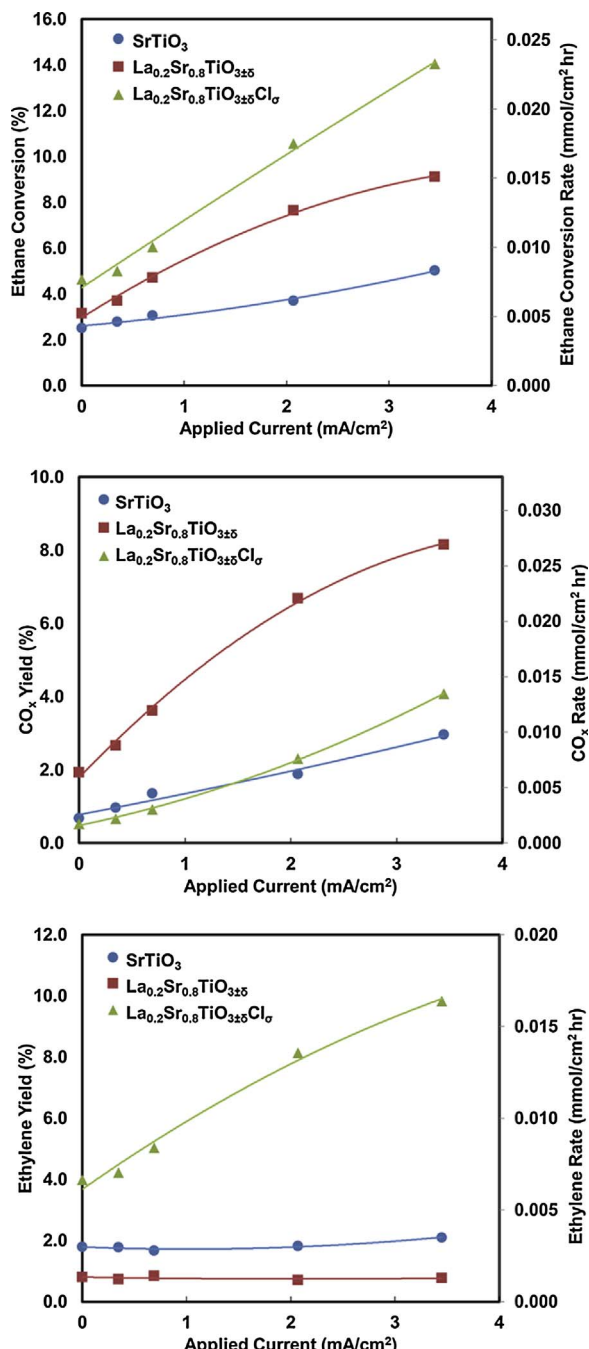


Fig. 14. Electrocatalytic activity of SrTiO₃, La_{0.2}Sr_{0.8}TiO_{3±δ}, and La_{0.2}Sr_{0.8}TiO_{3±δ}Cl_σ (Electrode geometric surface area = 1.5 cm²).

range. This may be due to the extremely low electrical conductivity of SrTiO₃ under reducing environment, as well as the lower electrochemical activity towards ethane conversion as seen from the gas chromatography data.

AC impedance spectroscopy was also performed on the operating cells under different applied currents. Fig. 16 shows the Nyquist impedance plots for cells with SrTiO₃, La_{0.2}Sr_{0.8}TiO_{3±δ}, and La_{0.2}Sr_{0.8}TiO_{3±δ}Cl_σ anodes under 0.5 mA and 1 mA current. The low frequency semicircle feature to the right appears to be relatively constant regardless of the anode and slightly decreases with increasing constant current, we attribute this to the cathode reaction, which in this case was the reduction of O₂ on LSM. Since all cells have the same cathode they were expected to have similar resistance behavior. The higher frequency semicircle may be attributed to the anode reaction. A

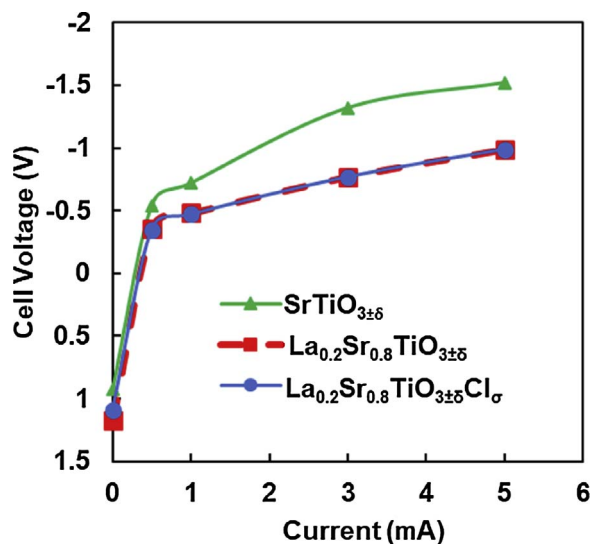


Fig. 15. Current-Voltage relationship of solid oxide cells with SrTiO₃, La_{0.2}Sr_{0.8}TiO_{3±δ}, and La_{0.2}Sr_{0.8}TiO_{3±δ}Cl_σ anodes.

comparison between the Nyquist plot shows that La_{0.2}Sr_{0.8}TiO_{3±δ} anode is the least resistive of the catalysts compared, while the cell with an undoped SrTiO₃ anode had the highest. These results are in good agreement with our electrical conductivity measurements that were made on dense catalyst pellets. From the impedance data, it was also observed that the total resistance decreases with increasing current (shown for La_{0.2}Sr_{0.8}TiO_{3±δ}Cl_σ, Fig. 17). This could be due to better charge transfer at the electrode/electrolyte interfaces, easier oxygen ion transport and higher reaction rates [102]. However, the nature of the high frequency and low frequency features in the impedance cannot be completely confirmed with the data obtained during this study. A more in depth, systematic impedance measurement is needed to fully explain the decrease in the total resistances with increased current and the nature of the impedance features from their current responses.

4. Conclusions

In this study, ethylene was produced via electrocatalytically-assisted oxidative dehydrogenation of ethane using oxide ion-conducting electrolytes and strontium titanate perovskite anode catalysts. Strontium titanate-based perovskite materials showed promising results as anode catalysts for this process. It was observed that lanthanum doping in strontium titanates improved the conductivity of the material by orders of magnitude, and also increased the conversion rates of ethane. Chlorine incorporation to lanthanum-doped strontium titanate, on the other hand, decreased the conductivity slightly, but increased the conversion and ethylene selectivity significantly. XPS results suggested that Cl ions are replacing O ions and are more concentrated near the surface. It was also seen that lanthanum doping and chlorine incorporation greatly enhanced the catalytic activity and ethylene selectivity of strontium titanate catalyst for electrocatalytically-assisted oxidative dehydrogenation. It was also observed that both with lanthanum doping and chlorine incorporation oxygen mobility increased. Moreover, DRIFTS studies showed that La_{0.2}Sr_{0.8}TiO_{3±δ}Cl_σ catalyst has weaker, but a higher abundance of Lewis acid sites as well as more Brønsted acid sites. These changes in oxygen mobility and surface acidity may be related to the increased conversion and selectivities observed for La_{0.2}Sr_{0.8}TiO_{3±δ}Cl_σ; however further investigation is needed to fully understand the reasons for this improvement, and this is a part of an ongoing study.

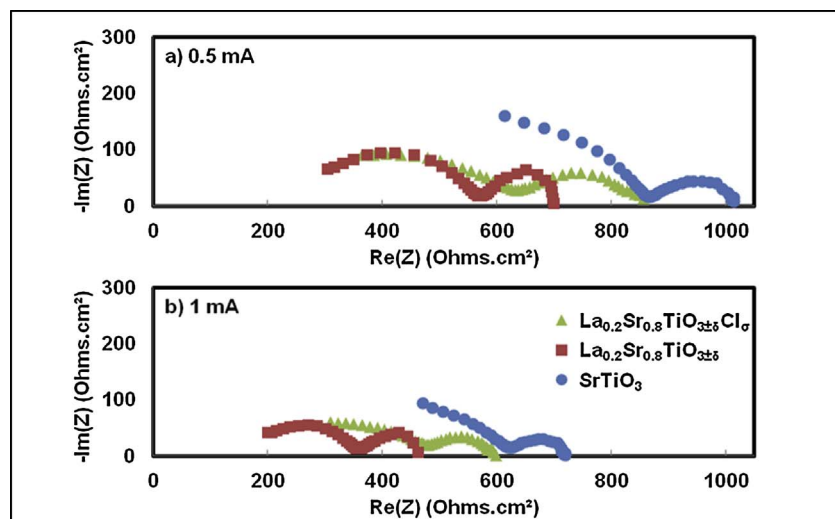


Fig. 16. Nyquist AC impedance plots at a) 0.5 mA, b) 1 mA for SrTiO_3 , $\text{La}_{0.2}\text{Sr}_{0.8}\text{TiO}_{3\pm\delta}$, and $\text{La}_{0.2}\text{Sr}_{0.8}\text{TiO}_{3\pm\delta}\text{Cl}_0$.

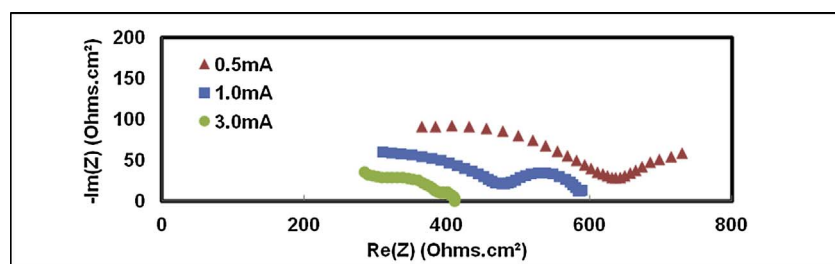


Fig. 17. Nyquist AC impedance plots for $\text{La}_{0.2}\text{Sr}_{0.8}\text{TiO}_{3\pm\delta}\text{Cl}_0$ at 0.5, 1, and 3 mA.

Acknowledgements

The financial support provided by the National Science Foundation through the Grant CHE-1213443 is gratefully acknowledged. The authors also acknowledge the Dr. Patricia Morris and her group for facilitating the screen printing to make the electrochemical cells tested in this work.

Appendix A. Supplementary data

Supplementary data associated with this article can be found, in the online version, at <https://doi.org/10.1016/j.apcatb.2018.01.019>.

References

- [1] T. Ren, M. Patel, K. Blok, Olefins from conventional and heavy feedstocks: energy use in steam cracking and alternative processes, *Energy* 31 (4) (2006) 425–451.
- [2] J.J.H.B. Sattler, et al., Catalytic dehydrogenation of light alkanes on metals and metal oxides, *Chem. Rev.* 114 (20) (2014) 10613–10653.
- [3] F. Cavani, F. Trifirò, The oxidative dehydrogenation of ethane and propane as an alternative way for the production of light olefins, *Catal. Today* 24 (3) (1995) 307–313.
- [4] H.H. Kung, Oxidative dehydrogenation of light (C2 to C4) alkanes, *Adv. Catal.* 40 (1994) 1–38.
- [5] G. Centi, F. Cavani, F. Trifirò, Selective Oxidation by Heterogeneous Catalysis, Kluwer/Plenum Publ., 2001 (p. 505-pp).
- [6] R. Grabowski, Kinetics of oxidative dehydrogenation of C2-C3 alkanes on oxide catalysts, *Catal. Rev.* 48 (2) (2006) 199–268.
- [7] R.B. Watson, S.L. Lashbrook, U.S. Ozkan, Chlorine modification of Mo/silica-titania mixed-oxide catalysts for the oxidative dehydrogenation of ethane, *J. Mol. Catal. A: Chem.* 208 (1-2) (2004) 233–244.
- [8] R.B. Watson, U.S. Ozkan, Mo loading effects over Mo/Si: Ti catalysts in the oxidative dehydrogenation of ethane, *J. Catal.* 208 (1) (2002) 124–138.
- [9] M.M. Bhasin, et al., Dehydrogenation and oxydehydrogenation of paraffins to olefins, *Appl. Catal. A: Gen.* 221 (1-2) (2001) 397–419.
- [10] M.M. Bhasin, Is true ethane oxydehydrogenation feasible? *Top. Catal.* 23 (1-4) (2003) 145–149.
- [11] H.H. Kung, M.C. Kung, Oxidative dehydrogenation of alkanes over vanadium-magnesium-oxides, *Appl. Catal. A: Gen.* 157 (1) (1997) 105–116.
- [12] M.P. Woods, B. Mirkelamoglu, U.S. Ozkan, Oxygen and nitrous oxide as oxidants: implications for ethane oxidative dehydrogenation over silica-titania-supported molybdenum, *J. Phys. Chem. C* 113 (23) (2009) 10112–10119.
- [13] H.G. Lintz, A. Reitzmann, Alternative reaction engineering concepts in partial oxidations on oxido catalysts, *Catal. Rev.* 49 (1) (2007) 1–32.
- [14] A.L.Y. Tonkovich, et al., Experimental investigations of inorganic membrane reactors: a distributed feed approach for partial oxidation reactions, *Chem. Eng. Sci.* 51 (5) (1996) 789–806.
- [15] Y. Ben Taarit, J.H. Lunsford, EPR evidence for $^{17}\text{O}^-$ on molybdenum oxide supported by silica-gel, *Chem. Phys. Lett.* 19 (3) (1973) 348–350.
- [16] M.B. Ward, M.J. Lin, J.H. Lunsford, The oxidative dehydrogenation of ethane by nitrous oxide over molybdenum oxide supported on silica gel, *J. Catal.* 50 (2) (1977) 306–318.
- [17] M. Iwamoto, T. Taga, S. Kagawa, Selective dehydrogenation of ethane by nitrous oxide over various metal oxide catalysts, *Chem. Lett.* 11 (9) (1982) 1469–1472.
- [18] K.-I. Aika, et al., Kinetics and mechanism of oxidative dehydrogenation of ethane and small alkanes with nitrous oxide over cobalt-doped magnesium oxide, *J. Chem. Soc. Faraday Trans. 1: Phys. Chem. Condens. Phases* 83 (10) (1987) 3139–3148.
- [19] S. Hamakawa, et al., Selective oxidation of ethane using the Au|YSZ|Ag electrochemical membrane system, *J. Electrochem. Soc.* 144 (1) (1997) 1–5.
- [20] E. Subbarao, Solid Electrolytes and Their Applications, Plenum Press, 1980 (p. 298-pp).
- [21] J. Coronas, M. Menendez, J. Santamaría, Use of a ceramic membrane reactor for the oxidative dehydrogenation of ethane to ethylene and higher hydrocarbons, *Ind. Eng. Chem. Res.* 34 (12) (1995) 4229–4234.
- [22] K. Sundmacher, L.K. Rihko-Struckmann, V. Galvita, Solid electrolyte membrane reactors: status and trends, *Catal. Today* 104 (2–4) (2005) 185–199.
- [23] T. Seiyama, Total oxidation of hydrocarbons on perovskite oxides, in: L.G. Tejada, J.L.G. Fierro (Eds.), Properties and Applications of Perovskite-type Oxides, CRC Press, 1993 (p. 215).
- [24] B. Viswanathan, CO oxidation and NO reduction on perovskite oxides, in: L.G. Tejada, J.L.G. Fierro (Eds.), Properties and Applications of Perovskite-type Oxides, CRC Press, 1993 (p. 271).
- [25] J. Haber, Concepts in catalysis by transition metal oxides, in: J.P. Bonnelle, B. Delmon, E.G. Deruelle (Eds.), Surface Properties and Catalysis by Non-metals, Reidel, Dordrecht, 1983.
- [26] H.X. Dai, C.F. Ng, C.T. Au, Perovskite-type chloro-oxide $\text{SrCoO}_{3.8}\text{Cl}_0$: a novel and durable catalyst for the selective oxidation of ethane to ethene, in: F.V.M.S.M. Avelino Corma, G.F. José Luis (Eds.), Studies in Surface Science and Catalysis, Elsevier, 1762, pp. 1757–1762.
- [27] G.J. Hutchings, M.S. Scurrell, J.R. Woodhouse, Partial oxidation of methane over samarium and lanthanum oxides: a study of the reaction mechanism, *Catal. Today* 4 (3-4) (1989) 371–381.
- [28] K. Aika, J.H. Lunsford, Surface reactions of oxygen ions. 2. Oxidation of alkenes by O^- on MgO, *J. Phys. Chem.* 82 (16) (1978) 1794–1800.
- [29] K. Aika, J.H. Lunsford, Surface reactions of oxygen ions. 1. Dehydrogenation of alkanes by O^- on MgO, *J. Phys. Chem.* 81 (14) (1977) 1393–1398.
- [30] D.J. Driscoll, et al., Formation of gas-phase methyl radicals over MgO, *J. Am.*

Chem. Soc. 107 (1) (1985) 58–63.

[31] M. Iwamoto, J.H. Lunsford, Surface reactions of oxygen ions. 5. Oxidation of alkanes and alkenes by O²⁻ on MgO, *J. Phys. Chem.* 84 (23) (1980) 3079–3084.

[32] Y. Takita, J.H. Lunsford, Surface reactions of oxygen ions. 3. Oxidation of alkanes by O³⁻ on MgO, *J. Phys. Chem.* 83 (6) (1979) 683–688.

[33] J.X. Wang, J.H. Lunsford, Characterization of [Li⁺ O²⁻] centers in lithium-doped MgO catalysts, *J. Phys. Chem.* 90 (22) (1986) 5883–5887.

[34] C.T. Au, X.P. Zhou, H.L. Wan, The activation of O₂ and the oxidative dehydrogenation of C₂H₆ over SmOF catalyst, *Catal. Lett.* 40 (1996) 101–104.

[35] Y. Osada, et al., Oxidative coupling of methane over Y₂O₃-CaO catalysts, *Appl. Catal.* 59 (1990) 59–74.

[36] C.H. Lin, et al., Oxidative dimerization of methane over lanthanum oxide, *J. Phys. Chem.* 90 (4) (1986) 534–537.

[37] H.X. Dai, et al., The performances and characterization of BaO- and BaX₂ (X=F, Cl, and Br)-promoted Y2O3 catalysts for the selective oxidation of ethane to ethene, *J. Catal.* 187 (1) (1999) 59–76.

[38] T. Hayakawa, et al., Partial oxidation of ethane into acetaldehyde by active oxygen generated electrochemically on gold through yttria-stabilized zirconia, *J. Chem. Soc. Chem. Commun.* 15 (1994) 1743–1744.

[39] A.P.E. York, et al., Partial oxidation of C₂-C₄ alkanes into oxygenates using an Au | yttria-stabilized zirconia | Ag electrochemical reaction cell, *Journal of the Chemical Society, Faraday Trans.* 92 (19) (1996) 3579–3586.

[40] K. Takehira, et al., Oxidation of lower alkanes over MoO₃-V₂O₅ supported on YSZ-aided membrane reactor, *Desalination* 144 (1) (2002) 425–426.

[41] A.J. Jacobson, Materials for solid oxide fuel cells, *Chem. Mater.* 22 (3) (2010) 660–674.

[42] X. Zhou, et al., Progress in La-doped SrTiO₃ (LST)-based anode materials for solid oxide fuel cells, *RSC Adv.* 4 (1) (2014) 118–131.

[43] M. Gong, et al., Sulfur-tolerant anode materials for solid oxide fuel cell application, *J. Power Sources* 168 (2) (2007) 289–298.

[44] R. Mukundan, E.L. Brosha, F.H. Garzon, Sulfur tolerant anodes for SOFCs, *Electrochem. Solid State Lett.* 7 (1) (2004) A5–A7.

[45] H. He, J.M. Vohs, R.J. Gorte, Carbonaceous deposits in direct utilization hydrocarbon SOFC anode, *J. Power Sources* 144 (1) (2005) 135–140.

[46] J.B. Goodenough, Y.-H. Huang, Alternative anode materials for solid oxide fuel cells, *J. Power Sources* 173 (1) (2007) 1–10.

[47] M.A. Bañares, Supported metal oxide and other catalysts for ethane conversion: a review, *Catal. Today* 51 (2) (1999) 319–348.

[48] M. Baerns, O. Buyevskaya, Simple chemical processes based on low molecular-mass alkanes as chemical feedstocks, *Catal. Today* 45 (1–4) (1998) 13–22.

[49] H.X. Dai, C.F. Ng, C.T. Au, Perovskite-type halo-oxide La_{1-x}Sr_xFeO₃–_xX_o (X = F, Cl) catalysts selective for the oxidation of ethane to ethene, *J. Catal.* 189 (1) (2000) 52–62.

[50] X. Lu, et al., Modified Pechini synthesis and characterization of Y-doped strontium titanate perovskite, *Solid State Ionics* 178 (19–20) (2007) 1195–1199.

[51] J.G. McCarty, H. Wise, Perovskite catalysts for methane combustion, *Catal. Today* 8 (2) (1990) 231–248.

[52] M.E. Bowden, D.A. Jefferson, I.W.M. Brown, Determination of layer structure in Sr_{1-x}La_xTiO_{3+0.5x} (0 < x < 1) compounds by high-resolution electron microscopy, *J. Solid State Chem.* 117 (1995) 88–96.

[53] S. Hashimoto, et al., A study on the structural and electrical properties of lanthanum-doped strontium titanate prepared in air, *J. Alloys Compd.* 397 (1–2) (2005) 245–249.

[54] C. Périllat-Merceroz, et al., New insights on the structure and reducibility of 3D versus 2D La/Sr titanates for SOFC anodes, *Solid State Ionics* 247 (-248) (2013) 76–85.

[55] R. Moos, et al., Solubility of lanthanum in strontium titanate in oxygen-rich atmospheres, *J. Mater. Sci.* 32 (1997) 4247–4252.

[56] N.G. Eror, U. Balachandran, Self-compensation in lanthanum-doped strontium titanate, *J. Solid State Chem.* 40 (1981) 85–91.

[57] S.B. Adler, Factors governing oxygen reduction in solid oxide fuel cell cathodes, *Chem. Rev.* 104 (10) (2004) 4791–4844.

[58] S. Hashimoto, et al., A study on the structural and electrical properties of lanthanum-doped strontium titanate prepared in air, *J. Alloys Compd.* 397 (1–2) (2005) 245–249.

[59] O.A. Marina, N.L. Canfield, J.W. Stevenson, Thermal, electrical, and electrocatalytical properties of lanthanum-doped strontium titanate, *Solid State Ionics* 149 (1–2) (2002) 21–28.

[60] S. Hashimoto, F.W. Poulsen, M. Mogensen, Conductivity of SrTiO₃ based oxides in the reducing atmosphere at high temperature, *J. Alloys Comps.* 439 (1–2) (2007) 232–236.

[61] B.-K. Park, et al., La-doped SrTiO₃ interconnect materials for anode-supported flat-tubular solid oxide fuel cells, *Int. J. Hydrogen Energy* 37 (5) (2012) 4319–4327.

[62] S. Lee, et al., SOFC anodes based on infiltration of La_{0.6}Sr_{0.7}TiO₃, *J. Electrochem. Soc.* 155 (11) (2008) B1179–B1183.

[63] C. Liu, U.S. Ozkan, Spectroscopic and structural characterization of chlorine loading effects on Mo/Si:Ti catalysts in oxidative dehydrogenation of ethane, *J. Phys. Chem. A* 109 (6) (2005) 1260–1268.

[64] M.M. Bettahar, et al., On the partial oxidation of propane and propylene on mixed metal oxide catalysts, *Appl. Catal. A: Gen.* 145 (1) (1996) 1–48.

[65] G.W. Keulks, The mechanism of oxygen atom incorporation into the products of propylene oxidation over bismuth molybdate, *J. Catal.* 19 (2) (1970) 232–235.

[66] L.D. Krenzke, G.W. Keulks, The catalytic oxidation of propylene, *J. Catal.* 61 (2) (1980) 316–325.

[67] E.V. Hoefs, J.R. Monnier, G.W. Keulks, The investigation of the type of active oxygen for the oxidation of propylene over bismuth molybdate catalysts using infrared and Raman spectroscopy, *J. Catal.* 57 (2) (1979) 331–337.

[68] R.D. Wragg, P.G. Ashmore, J.A. Hockey, Selective oxidation of propene over bismuth molybdate catalysts: the oxidation of propene using ¹⁸O labeled oxygen and catalyst, *J. Catal.* 22 (1) (1971) 49–53.

[69] N. Lakshminarayanan, et al., Doped LaFeO₃ as SOFC catalysts: control of oxygen mobility and oxidation activity, *Catal. Today* 157 (1–4) (2010) 446–450.

[70] S.B. Adler, Mechanism and kinetics of oxygen reduction on porous La_{1-x}Sr_xCoO_{3-δ} electrodes, *Solid State Ionics* 111 (1–2) (1998) 125–134.

[71] G.B. Sun, et al., A crucial role of surface oxygen mobility on nanocrystalline Y₂O₃ support for oxidative steam reforming of ethanol to hydrogen over Ni/Y₂O₃ catalysts, *Appl. Catal. B: Environ.* 81 (3–4) (2008) 303–312.

[72] S. Royer, D. Duprez, S. Kaliaguine, Oxygen mobility in LaCoO₃ perovskites, *Catal. Today* 112 (1–4) (2006) 99–102.

[73] H. Song, U.S. Ozkan, Changing the oxygen mobility in Co/ceria catalysts by Ca incorporation: implications for ethanol steam reforming, *J. Phys. Chem. A* 114 (2010) 3796–3801.

[74] W.-D. Yang, X-ray photoelectron spectroscopy and electrical properties studies of La₂O₃-doped strontium titanate ceramics prepared by sol-precipitation method, *J. Mater. Sci.* 34 (14) (1999) 3533–3544.

[75] J. Faye, et al., Influence of lanthanum stoichiometry in La_{1-x}FeO_{3-δ} perovskites on their structure and catalytic performance in CH₄ total oxidation, *Appl. Catal. B: Environ.* 126 (2012) 134–143.

[76] C.N. Borca, et al., Analysis of the electronic configuration of the pulsed laser deposited La_{0.7}Ca_{0.3}MnO₃ thin films, *Appl. Surf. Sci.* 254 (4) (2007) 1352–1355.

[77] E.e. Beyreuther, XPS investigation of Mn valence in lanthanum manganite thin films under variation of oxygen content, *Phys. Rev. B* 73 (15) (2006) 155425.

[78] A. Ito, H. Masumoto, T. Goto, Microstructure and electrical conductivity of SrRuO₃ thin films prepared by laser ablation, *Materi. Trans.* 47 (11) (2006) 2808–2814.

[79] T. Yu, et al., Enhanced photoelectrochemical performance of coaxial-nanocoupled strontium-rich SrTiO₃/TiO₂ (001) nanotube arrays, *Ind. Eng. Chem. Res.* 54 (33) (2015) 8193–8200.

[80] J.D. et al. Baniecki, Surface core-level shifts of strontium observed in photoemission of barium strontium titanate thin films, *Appl. Phys. Lett.* 89 (16) (2006) 162908.

[81] P.V. Nagarkar, P.C. Seaton, F.D. Gealy, Effect of surface treatment on SrTiO₃: an x-ray photoelectron spectroscopic study, *J. Appl. Phys.* 69 (1) (1991) 459–462.

[82] H. Xu, et al., Hierarchical chlorine-doped rutile TiO₂ spherical clusters of nanorods: large-scale synthesis and high photocatalytic activity, *J. Solid State Chem.* 181 (9) (2008) 2516–2522.

[83] U. Yoshinori, et al., X-ray photoelectron spectroscopy of rare earth halides, *Bull. Chem. Soc. Jpn.* 59 (7) (1986) 2263–2267.

[84] V.V. Atuchin, et al., Electronic structure of layered ferroelectric high- k titanate La₂Ti₂O₇, *J. Phys. D: Appl. Phys.* 42 (3) (2009) 035305.

[85] R.O. Idem, S.P.R. Katikaneni, N.N. Bakhti, Catalytic conversion of canola oil to fuels and chemicals: roles of catalyst acidity, basicity and shape selectivity on product distribution, *Fuel Process. Technol.* 51 (1997) 101–125.

[86] S.-H. Chai, et al., Sustainable production of acrolein: investigation of solid acid-base catalysts for gas-phase dehydration of glycerol, *Green Chem.* 9 (10) (2007) (p. 1130).

[87] J.B. Rawlings, J.G. Ekerdt, *Chemical Reactor Analysis and Design Fundamentals*, Nob Hill Publishing, 2012, 2018.

[88] M. Badlani, I.E. Wachs, Methanol: a smart chemical probe molecule, *Catal. Lett.* 75 (3–4) (2001) 137–149.

[89] F. Benaliouche, et al., NH₃-TPD and FTIR spectroscopy of pyridine adsorption studies for characterization of Ag- and Cu-exchanged X zeolites, *Microporous Mesoporous Mater.* 111 (1–3) (2008) 80–88.

[90] E.P. Parry, An infrared study of pyridine adsorbed on acidic solids: characterization of surface acidity, *J. Catal.* 2 (5) (1963) 371–379.

[91] N. Lakshminarayanan, et al., Effect of additional B-site transition metal doping on oxygen transport and activation characteristics in La_{0.6}Sr_{0.4}(Co_{0.18}Fe_{0.72}X_{0.1})O_{3-δ} (where X = Zn, Ni or Cu) perovskite oxides, *Appl. Catal. B: Environ.* 103 (3–4) (2011) 318–325.

[92] J.N. Kuhn, U.S. Ozkan, Surface properties of Sr- and Co-doped LaFeO₃, *J. Catal.* 253 (1) (2008) 200–211.

[93] Z. Skoufa, E. Heracleous, A.A. Lemonidou, On ethane ODH mechanism and nature of active sites over Ni-based catalysts via isotopic labeling and methanol sorption studies, *J. Catal.* 322 (2015) 118–129.

[94] M.I. Zaki, et al., In situ FTIR spectra of pyridine adsorbed on SiO₂-Al₂O₃, TiO₂, ZrO₂ and CeO₂: general considerations for the identification of acid sites on surfaces of finely divided metal oxides, *Coll. Surf. A* 190 (3) (2001) 261–274.

[95] J. Lu, et al., Surface acidity and properties of TiO₂/SiO₂ catalysts prepared by atomic layer deposition: UV-visible diffuse reflectance, DRIFTS, and visible raman spectroscopy studies, *J. Phys. Chem. C* 113 (28) (2009) 12412–12418.

[96] P. Ren, N. Masó, A.R. West, Hole conductivity in oxygen-excess BaTi_{1-x}Ca_xO_{3-x+δ}, *Phys. Chem. Chem. Phys.* 15 (48) (2013) 20943.

[97] S.C. Middleburgh, et al., Peroxide defect formation in zirconate perovskites, *J. Mater. Chem. A* 2 (2014) 15883–15888.

[98] M.D. Argyle, et al., Effect of catalyst structure on oxidative dehydrogenation of ethane and propane on alumina-supported vanadia, *J. Catal.* 208 (2002) 139–149.

[99] O. Desponts, R.L. Keiski, G.A. Somorjai, The oxidative dehydrogenation of ethane over molybdenum-vanadium-niobium oxide catalysts: the role of catalyst composition, *Catal. Lett.* 19 (1993) 17–32.

[100] E. Heracleous, et al., Oxidative dehydrogenation of ethane and propane over vanadia and molybdena supported catalysts, *J. Mol. Catal. A: Chem.* 232 (2005) 29–39.

[101] E. Morales, J.H. Lunsford, Oxidative dehydrogenation of ethane over a lithium-promoted magnesium oxide catalyst, *J. Catal.* 118 (1989) 255–265.

[102] A. Nechache, et al., Diagnosis of a cathode-supported solid oxide electrolysis cell by electrochemical impedance spectroscopy, *Electrochim. Acta* 210 (2016) 596–605.